

# MedRegion-CT: Region-Focused Multimodal LLM for Comprehensive 3D CT Report Generation

Sunggu Kyung, Jinyoung Seo, Hyunseok Lim, Dongyeong Kim, Hyungbin Park,  
Jimin Sung, Jihyun Kim, Wooyoung Jo, Yoojin Nam, Namkug Kim  
Department of Bioengineering, University of Ulsan College of Medicine, Asan Medical Center  
babbu3682@gmail.com, namkugkim@mail.ulsan.ac.kr

## Abstract

The recent release of RadGenome-Chest CT has significantly advanced CT-based report generation. However, existing methods primarily focus on global features, making it challenging to capture region-specific details, which may cause certain abnormalities to go unnoticed. To address this, we propose MedRegion-CT, a region-focused Multi-Modal Large Language Model (MLLM) framework, featuring three key innovations. First, we introduce Region Representative ( $R^2$ ) Token Pooling, which utilizes a 2D-wise pre-trained vision model to efficiently extract 3D CT features. This approach generates global tokens representing overall slice features and region tokens highlighting target areas, enabling the MLLM to process comprehensive information effectively. Second, a universal segmentation model generates pseudo-masks, which are then processed by a mask encoder to extract region-centric features. This allows the MLLM to focus on clinically relevant regions, using six pre-defined region masks. Third, we leverage segmentation results to extract patient-specific attributions, including organ size, diameter, and locations. These are converted into text prompts, enriching the MLLM’s understanding of patient-specific contexts. To ensure rigorous evaluation, we conducted benchmark experiments on report generation using the RadGenome-Chest CT. MedRegion-CT achieved state-of-the-art performance, outperforming existing methods in natural language generation quality and clinical relevance while maintaining interpretability. The code for our framework is publicly available.

## 1. Introduction

Computed tomography (CT) plays a crucial role in medical diagnostics, providing clinicians with detailed information about anatomical structures and pathological conditions [1]. Compared to 2D imaging, 3D CT captures spatial relationships and lesion details with higher precision,

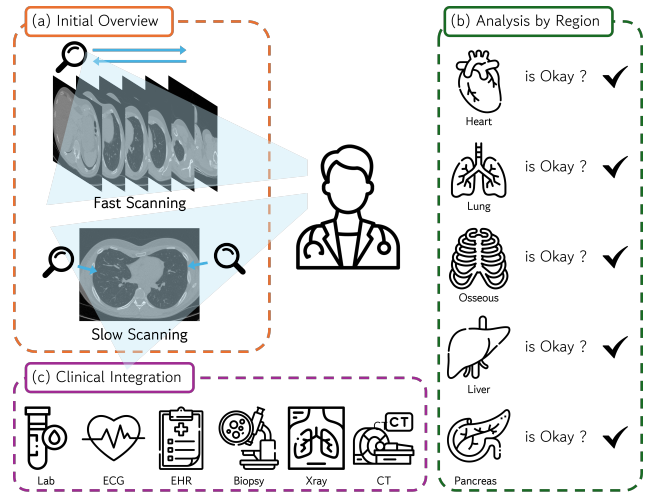


Figure 1. Comprehensive radiological workflow for clinical diagnosis. (a) Initial Overview: fast and slow scanning techniques for preliminary image review. (b) Analysis by Region: systematic assessment of major organ systems. (c) Clinical Integration: correlation with various medical information for comprehensive patient evaluation.

thereby enabling more accurate and comprehensive diagnoses. However, manually analyzing numerous CT slices and generating radiology reports is a time-consuming and labor-intensive task for radiologists [2, 3]. Therefore, the development of automated systems that enhance diagnostic quality while alleviating clinicians’ workload is essential.

Recent progress in Multi-Modal Large Language Models (MLLMs) [4–8] have facilitated the effective handling of complex multimodal tasks by leveraging the robust language understanding capabilities of large language models (LLMs). In line with these advancements, MLLMs in the medical domain have demonstrated the ability to comprehend medical images and relevant clinical information, enabling their application in report generation tasks.

Yet, most existing studies primarily focus on 2D med-

ical images, leaving the field of report generation for 3D data (e.g., CT, MRI) relatively unexplored. This limitation can be attributed to several technical challenges such as data scarcity, the complexity of feature extraction, and the high computational cost associated with processing large-scale datasets [9, 10].

The recent release of large-scale 3D CT datasets, such as CT-RATE [11] and RadGenome-Chest CT [12], has created new opportunities for advancements in 3D medical image analysis and report generation. Notably, open-source 3D medical MLLMs [13–17] have shown promising results in few tasks such as anomaly detection and context retrieval. However, these MLLMs predominantly rely on global volume-level features, which limits their ability to capture the fine-grained, region-specific details that are essential for report generation. To advance MLLMs towards generating diagnostically valuable CT reports, it is crucial to develop models that not only extract region-focused information effectively but also integrate it seamlessly into the report generation process.

Another challenge in analyzing 3D medical images is the absence of robust and well-optimized encoders. While 2D medical images share a similar data structure with natural images, allowing for transfer learning using pre-trained universal 2D encoders [18–20], 3D medical images differ significantly from natural images. This makes it difficult to directly apply existing encoders to 3D medical images. Inevitably, 3D encoders require extensive pre-training for medical imaging applications, which entails substantial computational costs.

Radiologists initially review CT scans on a slice-wise basis to perform a rapid holistic assessment, followed by a focused examination of specific slices where key organs are clearly visible, allowing them to extract detailed regional features critical for precise diagnosis (see Fig. 1-(a)). To effectively capture regional features in a similar manner, we introduce Region Representative ( $R^2$ ) Token Pooling. In this method, global tokens are constructed from visual tokens extracted from individual slices of a CT scan, while additional region tokens are derived from clinically informative slices. By incorporating these global tokens and representative region tokens, this framework enables to process 3d visual features efficiently.

After an initial overview, radiologists typically conduct organ-based analysis to obtain more detailed information (see Fig. 1-(b)). To emulate this analytical protocol, we introduce a Mask-Driven Visual Extractor for region-focused feature extraction. In this method, a universal segmentation model generates pseudo-masks for key organs. These pseudo-masks are processed through the mask driven extractor to extract mask tokens and spatial tokens, which are integrated into the LLM.

Additionally, radiologists make their diagnostic deci-

sions based on various medical information (see Fig. 1-(c)). We process the pseudo-masks of key organs and lesions through a deterministic algorithm to extract Patient-Specific Attributes (e.g., organ volume, diameter, lesion location), which are then incorporated into the LLM as textual prompts. This strategy enhances the precision and clinical relevance of the generated reports by providing personalized diagnostic insights.

In summary, we propose MedRegion-CT, an effective framework for generating 3D CT reports. In our experiments setting, MedRegion-CT achieves state-of-the-art performance in report generation tasks, surpassing existing methods in clinical validity and interpretability. The generated reports exhibit superior accuracy and coherence, significantly enhancing the framework’s applicability in real-world clinical settings. Our contributions are as follows:

- We introduce a Region Representative ( $R^2$ ) Token Pooling that efficiently extracts features from 3D CT images by leveraging pre-trained 2D vision models, generating region tokens focused on clinically informative slices, as well as global tokens representing the entire scan.
- We propose Mask-Driven Visual Extractor that processes the pseudo-masks generated by the universal segmentation model to extract region-focused features, allowing LLM to capture localized information of the region.
- We extract Patient-Specific Attributes from the pseudo-masks and convert them into textual prompts, enhancing the LLM’s contextual understanding of the individual case.

## 2. Related Work

### 2.1. Medical MLLMs.

Recent advancements in MLLMs have demonstrated competent performance by employing LLM as decoders and using instruction-following sets [21]. 2D medical MLLMs [22–30] have been developed by finetuning open source LLMs and using robust 2D vision models on large-scale paired medical image–text datasets [31–33]. These models have achieved remarkable performance across various medical applications, including report generation, visual question answering (VQA), and disease diagnosis.

Despite these advancements, the development of 3D medical MLLMs has been comparatively restricted, mainly due to limited suitable data. To address these challenges, Hamamci *et al.* [17] introduced the CT-RATE dataset, consisting of 26K chest CT volumes paired with their corresponding radiology reports. Wu *et al.* [13], Bai *et al.* [15] collected diverse 3D medical data from publicly accessible professional medical websites and tailored them for various 3D medical tasks. Recently, the release of RadGenome-Chest CT [12], a large-scale grounded dataset has opened new possibilities for further advancement in the field of 3D

MLLMs.

Currently, several open-source 3D medical MLLMs have been introduced. RadFM [13] is a pioneering radiology-based model that processes both 2D and 3D scans across multiple imaging modalities through its combined 3D ViT and Perceiver architecture. MedBLIP [14] further enhanced capabilities by incorporating EHR data and employing MedQFormer to adapt 3D images to pre-trained 2D encoders. CT2Rep [16] leveraged 3D Auto-regressive Transformers and memory-driven decoders to effectively process longitudinal data. M3D [15] employed 3D ViT encoders with spatial pooling perceivers to compress high-dimensional tokens, while also enabling promptable segmentation. Despite these advancements, challenges remain in dataset diversity, computational optimization, and standardized evaluation.

## 2.2. 3D Vision Encoder for MLLMs.

In the 3D medical MLLM domain, extracting spatial features has long been a challenging task. Prior research commonly adopts one of two approaches. The first uses a 3D vision encoder like 3D ViT, which partitions an entire imaging volume into fixed-size 3D patches. Most MLLM models [13, 15, 34] depend on such 3D vision encoders. However, Due to the uniqueness of medical data (e.g., CT and MRI), these encoders often require pretraining from scratch and may fail to capture slice-level details.

The second approach extracts features from each 2D slice independently and then aggregates them. While this method benefits from pretrained 2D encoders, it can lose 3D context and inter-slice consistency. To address these issues, CT2Rep employs a CT-ViT [35] structure that groups selected slices before integrating them. MS-VLM [36] processes slices individually, then uses a  $z$ -former to efficiently aggregate slice-level features, whereas Med-2E3 [37] fuses features derived from both 3D and 2D encoders. Even if 3D features are successfully extracted, the high dimensionality and large number of tokens in 3D medical data can create a heavy computational burden when fed into the LLM. Inevitably, MLLM methods often compress vision features to reduce computational cost while retaining spatial relationships and detailed context.

Recently, the video editing domain has adopted a dual frame rate strategy—incorporating both slow and fast frames—to achieve more comprehensive content representation while significantly enhancing computational efficiency [38–40]. Inspired by the slow-fast architecture [41], we optimize computational efficiency by reinterpreting the concept of *fast* and *slow* tokens in the medical domain. Fast tokens were designed to provide depth information by embedding all slices while using fewer visual tokens per slice. In contrast, slow tokens, generated by embedding slices that represent key regions, capture rich local infor-

mation by employing more visual tokens per slice.

## 2.3. Region-Focused MLLMs.

Several studies [42–44] in general domains have explored the incorporation of local features into LLMs, demonstrating their potential for region-level understanding. However, region-level interpretation in medical imaging remains relatively underexplored. Most existing medical MLLMs process entire images as a single representation, making it difficult to generate text focusing on specific regions. Furthermore, medical reports often describe multiple regions simultaneously.

To help identify specific clinically important regions, several studies fine-tuned models using instruction-following sets composed of Refer-and-Ground Conversations that utilize bounding-box-based coordinate information [45–47]. These datasets enable models to focus on specific regions, supporting object detection and grounded radiology report generation. MAIRA-2 [48] proposed the Grounded Radiology Report Generation task, utilizing datasets that provide annotated locations corresponding to each finding in chest X-rays (CXR). A few studies [49, 50] have focused on utilizing region-of-interest (ROI)-aligned features and integrating it into the LLM. For instance, RGRG [49] employs a detector to extract ROI features for CXR report generation, allowing for more fine-grained descriptions. Recently, semantic segmentation-based approaches have been explored to provide LLMs with pixel-level features. MAIRA-SEG [28] uses mask-aware visual extractor proposed in Osprey [51] to extract segmentation tokens from major organ and lesion pseudo-masks obtained by expert models. These segmentation tokens are then combined with CXR images to serve as input for the LLM. Similarly, Reg2RG [52] utilizes universal segmentation models [53] to extract organ pseudo-masks from CT images, preserving geometric information while retaining texture features in local embeddings. These local features are subsequently combined with global features to establish a coherent contextual understanding.

Building on these prior studies, we adopt SAT [53], a universal segmentation model, to extract pseudo-masks and propose a framework that effectively integrates semantic segmentation information.

## 2.4. Extention of Textual Prompts

Prompts were originally introduced as a natural language processing technique to improve the generalization of language models [54]. This method allows a language model to contextualize its inputs through text templates, thereby improving its ability to adapt to diverse tasks. Recent critical analyses of MLLMs have highlighted issues such as hallucination and reasoning errors induced by the transmission of visual features. [55, 56].

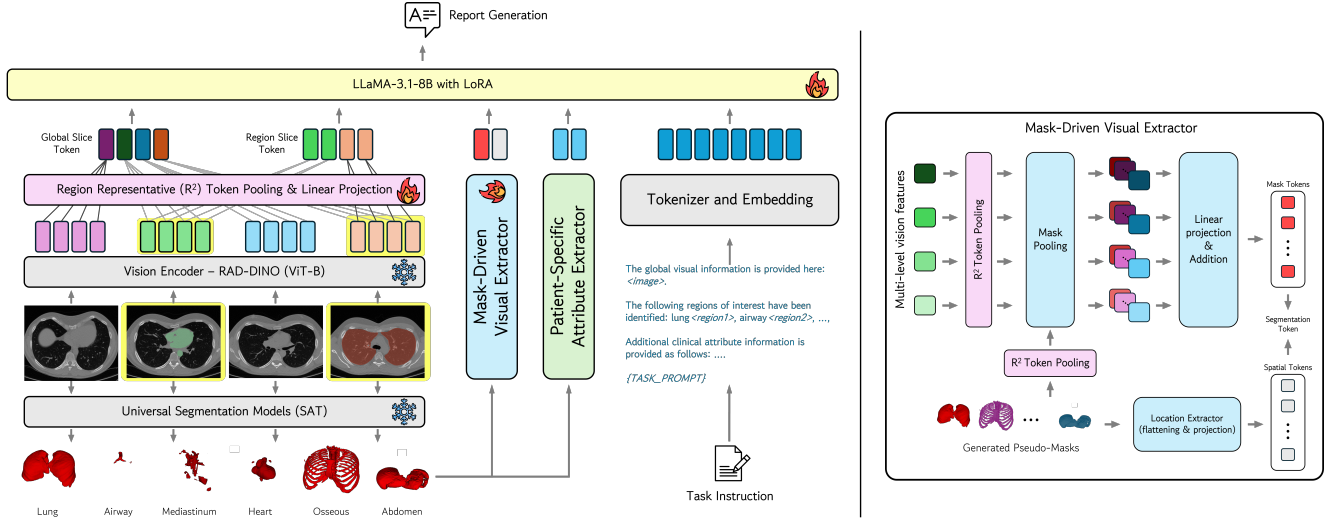


Figure 2. Overview of **MedRegion-CT**. In  $R^2$  token pooling, CT images processed in slice-wise independent manner undergo efficient feature extraction, yielding 3D vision tokens composed of global tokens and region representative tokens. Pseudo-masks are tokenized through  $R^2$  pooling to correspond with Multi Level visual tokens, and these are subsequently combined via mask pooling. Spatial tokens are derived from pseudo-masks through a location extractor. These two types of token collectively form the segmentation tokens. The patient-specific attribute extractor derives key morphological characteristics unique to each lesion from pseudo-masks. These three types of tokens are fed into an LLM to perform report generation along with a prompt.

To address these challenges, various methods utilizing prompts have been proposed. Qin *et al.* [57] leverages a pre-trained vision–language model to automatically construct medical prompts encompassing various graphical attributes such as color, texture, and shape. PromptMRG [58] is a pioneering study in introducing prompts to the medical report generation task, converting diagnostic outcomes into prompts. Dia-LLaMA [59] employs a disease-recognition attention module to extract disease-specific features from CT scan and classify the presence of each disease. The classification results are then transformed into diagnostic text prompts to guide the LLM. Insight [60] uses an instance-segmentation-based visual translator to convert meibography image into quantifiable morphological data, providing detailed insights in conjunction with clinical context. RadGPT [61] applies a deterministic algorithm to transform voxel-level annotations of tumors and organs into a structured report, thereby ensuring diagnostic consistency. Inspired by the methodology of RadGPT, we extracted supplementary clinical information from pseudo-mask and incorporated it into the LLM as textual input to enhance the quality of generated reports.

### 3. Method

**MedRegion-CT.** When generating a radiology report, radiologists typically analyze medical images region by region. Inspired by this workflow, MedRegion-CT generates reports for 6 predefined anatomical regions instead of pro-

ducing a full report. These individual region reports are subsequently merged to construct the final report. To align with this approach, we preprocessed the ground truth report by splitting them into the same predefined regions, creating a training set with the expected format. The architecture of MedRegion-CT is presented in Fig. 2. MedRegion-CT consists of 5 key elements: 1) 2D encoder for processing individual CT slices, 2)  $R^2$  Token Pooling that integrates features extracted at the slice level to construct 3D features, 3) Mask-Driven visual extractor, 4) Patient-Specific Attribute Extractor, 5) LLM.

We first employ a universal segmentation model to generate pseudo-masks for CT anatomical structures. These pseudo-masks serve as pseudo-labels for the MLLM. To extract visual features from each CT slice, we utilize a pre-trained 2D image encoder. We then integrate these features through  $R^2$  Token Pooling, a novel approach that combines global tokens and region-representative tokens to construct  $T_{vision}$ , the vision tokens of the image.  $T_{vision}$  is integrated with the pseudo-masks to input the Mask Driven Visual Extractor. The Mask Driven Visual Extractor generates mask tokens and spatial tokens, which collectively form segmentation tokens,  $T_{seg}$ . Additionally, medical information is extracted from the pseudo-masks using deterministic algorithms, which are then converted into patient-specific attribute text tokens  $T_{attr}$  for comprehensive representation of medical data.  $T_{vision}$ ,  $T_{seg}$ ,  $T_{attr}$  are provided as input to the LLM with instruction prompts  $I$ . The LLM generates the report  $R$ . This can be formulated as:

$$R = LLM(T_{vision}, T_{seg}, T_{attr}, I) \quad (1)$$

This enables the generation of precise medical reports focused on specific anatomical regions. The following sections provide detailed explanations of each element.

### 3.1. Structured Report Generation

To analyze chest CT scans in a structured way, we divide the anatomical field of view into 6 regions: 1) Lung, 2) Large airways, 3) Mediastinum, 4) Heart and great vessels, 5) Osseous structures, and 6) Upper Abdomen. This categorization reflects the methodical approach that radiologists use to interpret chest images, ensuring that each region is evaluated for relevant pathology [62]. Additionally, this structured approach contributes to the quality and consistency of radiology reports by facilitating comprehensive documentation of findings across all anatomical structures [63]. For segmentation of the six primary regions, our framework does not depend on a specific segmentation model and possesses a flexible architecture that facilitates the integration of various segmentation models as required.

### 3.2. 3D Vision Token Using $R^2$ Token Pooling

Generally, encoders using slice-wise strategies outputs  $D \times T$  tokens when processing 3D images ( $D$  is depth or the number of slices,  $T$  is the number of tokens per slice). While this approach would ideally involve all slices along the depth axis, directly inputting such large number of tokens to the LLM module requires substantial computational resources. To address this issue, we adopted the concepts of fast and slow tokens introduced in LITA [38] and generated global tokens and region representative tokens from 3D CT images.

Global tokens  $T_{glob}$  are densely sampled to provide slice depth information. We obtain one global token from each slice by averaging all visual tokens, resulting in a total of  $D$  global tokens. Region representative tokens  $T_{reg}$  are sparsely sampled to preserve more detailed spatial information. We select  $s$  slices from the CT, and for each slice, we performed spatial adaptive pooling to downsample the tokens by a factor of  $s$ . For each slice, we obtain  $\frac{T}{s}$  tokens, resulting in a total of  $T$  region representative tokens.

Unlike LITA [38], we applied a region-centric method for slow token sampling rather than uniform sampling. We sample representative slice for each region by selecting the slice with the highest number of pseudo-mask pixels.

The obtained  $T_{glob}$  and  $T_{reg}$  tokens are merged to construct the final 3D vision token.

$$T_{visual} = Concat(T_{global}, T_{region}) \quad (2)$$

This approach allows us to represent 3D CT with a total of  $D + T$  tokens, compared to  $D \times T$  tokens. This dramatically

reduces the token count while effectively preserving interslice relationships and spatial information.

### 3.3. Mask-Driven Visual Extractor

To extract mask features, MAIRA-SEG [28] utilizes the mask encoder of Osprey [51], with a transformer-based Rad-DINO (ViT-B backbone) [64]. We adopt the MAIRA-SEG’s mask aware visual extractor to obtain mask tokens and spatial tokens. Mask tokens are generated from multi level visual tokens and pseudo-masks by applying mask pooling and linear projections. Spatial tokens are derived from the pseudo-masks through flattening and linear projection. Mask tokens and spatial tokens are then concatenated to form segmentation tokens. This approach is highly efficient, as it generates only two segmentation tokens for each mask, making it well-suited for the LLM’s fixed computational capacity and context length. The extracted segmentation tokens are used to prompt the LLM along with image and text tokens.

Compared to MAIRA-SEG [28] which is restricted to 2D images, we expand this architecture to 3D. To mitigate the computational burden associated with 3D extension, we applied Mask-Driven Visual Extractor. Instead of directly utilizing multi-level image features, we adapts  $R^2$  token pooling in mask pooling operation as illustrated in Fig.2. Mask information tokenized through  $R^2$  token pooling is aligned with multi-level visual tokens to facilitate mask pooling.

Another key distinction from MAIRA-SEG [28] is our consistent placement of text and segmentation tokens in fixed positions, regardless of mask positivity. This enables direct recognition of segmentation information independent of prompt structure and facilitates extension to lesion masks by allowing autonomous assessment of lesion presence based on mask information.

Apart from the aforementioned modifications, we use the same hyperparameter settings as MAIRA-SEG, including the linear projector, embedding dimension size, specific layer output indices of the ViT-B-based encoder, and the number of segmentation tokens.

### 3.4. Patient Attribution Extractor

MLLMs have certain limitations in processing visual data through encoders, and there is a possibility of losing details during the cropping and resizing of CT images. To address this, we propose a method of extracting additional clinical information using pseudo-masks. In this study, inspired by the vision translator concept suggested in previous research [60, 61], we quantitatively extracted clinical information using deterministic algorithms. This transformation technique serves to integrate rich morphological details into the LLM by providing additional clinical metadata. We extracted (1) volumetric measurements for the lungs, heart, liver and kid-

Method	NLG Metrics			LM Based Metrics		
	BLEU-4	ROUGE-L	METEOR	CA-F1 score	Green score	GPT-4 score
CT2Rep [16]	0.242	0.347	0.431	0.305	<b>0.374</b>	44.508
RadFM [13]	0.262	0.365	0.489	0.350	0.234	46.178
MedBLIP [14]	0.279	0.373	0.494	0.370	0.215	46.825
M3D [15]	<u>0.288</u>	<b>0.391</b>	<b>0.497</b>	<u>0.435</u>	<u>0.297</u>	<u>47.243</u>
Ours (Ablation- $R^2$ +Attr+Mask)	<b>0.290</b>	<u>0.375</u>	<u>0.494</u>	<b>0.450</b>	0.278	<b>48.837</b>
Ablation- $R^2$ +Mask	0.280	0.367	0.498	0.430	0.264	44.457
Ablation- $R^2$ +Attr	0.293	0.375	0.489	0.425	0.282	47.319
Ablation- $R^2$	0.261	0.345	0.481	0.405	0.233	43.014
Ablation-LITA [38]	0.268	0.343	0.479	0.385	0.231	42.293

Table 1. Comparison of NLG\* Metrics and LM\* Based Metrics on the generated reports between MS-VLM and baseline methods. LM Based Metrics include CA-F1 score (averaged across 18 chest-related abnormalities), Green Score, and GPT-4 score. The best performance is highlighted in **bold** and the second-best is underlined. *LITA* [38] uniformly sample slices for slow tokens.  $R^2$  denotes our Region Representative ( $R^2$ ) Token Pooling, which sample slices for slow tokens with region-centric method. *Attr* denotes our Patient Attribution Extractor. *Mask* denotes our Mask-Driven Visual Extractor. \*NLG: Natural Language Generation, LM: Language Model.

ney, (2) count, diameter and spatial location data for lesions (nodules, effusion and cysts), as can be seen in Fig. 4. The extracted clinical information was subsequently restructured into patient-specific reports and delivered to the LLM in textual form, as shown in Fig. 5. This contributes to the generation of more reliable region-centric reports.

Measuring organ volumes and characterizing lesions yields clinically significant information across various disease states. In patients with idiopathic pulmonary fibrosis (IPF), lung volume progressively declines and demonstrates strong correlation with pulmonary function [65]. These volumetric measurements therefore serve as valuable quantitative biomarkers for both disease diagnosis and prognostic evaluation. Furthermore, the conversion of nodule masks and kidney cyst masks into textual attributes enhances radiologists’ interpretative capabilities [66, 67]. When represented as textual parameters, these measurements can facilitate more precise disease characterization and outcome prediction.

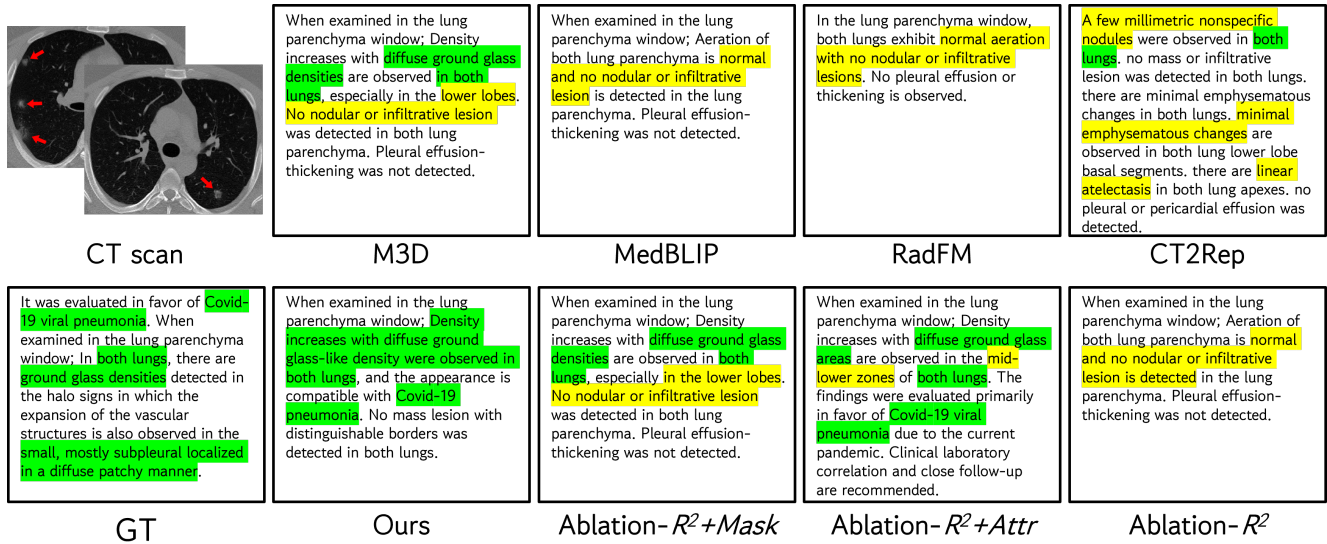
## 4. Experiment

### 4.1. Dataset and Evaluation Metric

**Dataset.** In our study, we utilized RadGenome-Chest CT [12], a comprehensive dataset designed for 3D chest CT interpretation. Built upon CT-RATE[17], this dataset contains 25,692 non-contrast chest CT volumes with corresponding radiology reports from approximately 20,000 patients. RadGenome-Chest CT provides detailed organ-level segmentation masks covering 197 anatomical regions, which were generated using SAT [53], the latest powerful text-prompted universal segmentation model. The dataset features 665K grounded reports where each sentence links to specific anatomical regions in the CT volumes through seg-

mentation masks. We merged these numerous anatomical regions into six clinically relevant regions that we defined for our research. For each of these six regions, we integrated the corresponding report sentences to create comprehensive region-specific reports, which we then used as ground truth text. We followed the official dataset division, with 20,000 patients (24,128 volumes) allocated to training/validation and 1,304 patients (1,564 volumes) for test.

**Evaluation Metric.** Evaluating generated radiology reports requires assessing both linguistic similarity and clinical accuracy. Our methodology incorporates two metric categories: 1) Natural Language Generation (NLG) Metrics include BLEU [68] (Bilingual Evaluation Understudy), which calculates n-gram precision between candidate and reference texts; ROUGE (Recall-Oriented Understudy for Gisting Evaluation) [69], which measures how much reference content appears in the candidate; and METEOR (Metric for Evaluation of Translation with Explicit Ordering) [70], which aligns words using exact matches, stemming, and synonyms. 2) Language Model (LM) Based Metrics consist of Clinical Accuracy (CA) metrics using RadBERT [71] from CT-CLIP [17], which assesses abnormality detection through F1 scores; and GREEN (Generative Radiology Report Evaluation and Error Notation) [72], which identifies and explains clinically significant errors. We also utilize LLMs as evaluators to assess generated content. We employed GPT-4o Mini as the evaluator model using prompt designs from M3D [15] to evaluate generated reports against ground truth, providing scores from 0-100 that reflect diagnostic reasoning and contextual accuracy. This integrated approach ensures comprehensive assessment across structural, linguistic, and clinical dimensions essential for radiology reporting.



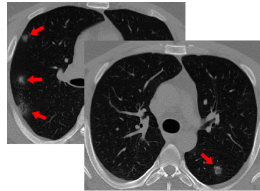
 <p>CT scan</p>	<p>When examined in the lung parenchyma window; Density increases with <b>diffuse ground glass densities</b> are observed in <b>both lungs</b>, especially in the lower lobes. <b>No nodular or infiltrative lesion</b> was detected in both lung parenchyma. Pleural effusion-thickening was not detected.</p> <p>M3D</p>	<p>When examined in the lung parenchyma window; Aeration of both lung parenchyma is <b>normal</b> and <b>no nodular or infiltrative lesion</b> is detected in the lung parenchyma. Pleural effusion-thickening was not detected.</p> <p>MedBLIP</p>	<p>In the lung parenchyma window, both lungs exhibit <b>normal aeration</b> with <b>no nodular or infiltrative lesions</b>. No pleural effusion or thickening is observed.</p> <p>RadFM</p>	<p>A few <b>millimetric nonspecific nodules</b> were observed in <b>both lungs</b>. no mass or infiltrative lesion was detected in both lungs. there are minimal emphysematous changes in both lungs. <b>minimal emphysematous changes</b> are observed in both lung lower lobe basal segments, there are <b>linear atelectasis</b> in both lung apices. no pleural or pericardial effusion was detected.</p> <p>CT2Rep</p>
<p>It was evaluated in favor of <b>Covid-19 viral pneumonia</b>. When examined in the lung parenchyma window; In <b>both lungs</b>, there are <b>ground glass densities</b> detected in the halo signs in which the expansion of the vascular structures is also observed in the <b>small, mostly subpleural localized in a diffuse patchy manner</b>.</p> <p>GT</p>	<p>When examined in the lung parenchyma window; Density increases with <b>diffuse ground glass-like density</b> were observed in <b>both lungs</b>, and the appearance is compatible with <b>Covid-19 pneumonia</b>. No mass lesion with distinguishable borders was detected in both lungs.</p> <p>Ours</p>	<p>When examined in the lung parenchyma window; Density increases with <b>diffuse ground glass densities</b> are observed in <b>both lungs</b>, especially in the lower lobes. <b>No nodular or infiltrative lesion</b> was detected in both lung parenchyma. Pleural effusion-thickening was not detected.</p> <p>Ablation-<math>R^2</math>+Mask</p>	<p>When examined in the lung parenchyma window; Density increases with <b>diffuse ground glass areas</b> are observed in the <b>mid-lower zones of both lungs</b>. The findings were evaluated primarily in favor of <b>Covid-19 viral pneumonia</b> due to the current pandemic. Clinical laboratory correlation and close follow-up are recommended.</p> <p>Ablation-<math>R^2</math>+Attr</p>	<p>When examined in the lung parenchyma window; Aeration of both lung parenchyma is <b>normal</b> and <b>no nodular or infiltrative lesion</b> is detected in the lung parenchyma. Pleural effusion-thickening was not detected.</p> <p>Ablation-<math>R^2</math></p>

Figure 3. Qualitative comparison of generated radiology reports for a patient with suspected COVID-19 pneumonia comparing previous works, our proposed model, and ablation studies (Ablation- $R^2$ +Mask, Ablation- $R^2$ +Attr, Ablation- $R^2$ ). Text is color-coded to highlight clinically important findings of ground-truth report (green) and erroneous findings of generated reports (yellow). MedRegion-CT demonstrates superior performance in both diagnostic accuracy and localization compared to previous works and ablation studies.

## 4.2. Quantitive and Qualitative Results

**Quantitative Results.** In this study, we comparatively evaluated five models for the radiology report generation task, including our proposed model (Ours), M3D, MedBLIP, RadFM, and CT2Rep. As shown in Table 1, our proposed model achieved the highest score among the five models in BLEU4 (0.290), as well as in CA (0.450) and GPT-4 score (48.837). These results suggest superior performance not only in lexical and structural similarity to reference reports but also in accurately conveying clinically essential information without distortion and minimizing unnecessary hallucinations. M3D demonstrated relatively stable performance through pretrained weights and multi-stage learning, showing competitive values in METEOR (0.497) and ROUGE-L (0.391). However, its CA and GPT-4 score were lower than our proposed model, indicating limitations in fully reflecting clinical accuracy. While both MedBLIP and RadFM utilize LLMs, MedBLIP, which employs pretrained models, exhibited relatively faster and more stable fine-tuning. Nevertheless, their overall performance did not match that of M3D or our proposed model. CT2Rep, due to its complex structure, could not incorporate LLMs and instead used an open-source framework trained from scratch. As a result, this relatively lightweight model was insufficiently trained with limited resources, leading to comparatively lower scores in most metrics including BLEU4, CA, and GPT-4 score. Although it achieved the highest Green Score (0.374), this was identified as a biased result primarily due to overfitting to normal cases, which constitute a

significant proportion of medical datasets. Collectively, our findings reveal that traditional NLG metrics alone are insufficient for fully measuring the clinical significance and diverse sentence expressions inherent in medical reports. The CA metric indicates clinical accuracy, while the GPT-4 score suggests more flexible contextual understanding and factual consistency. The fact that our proposed model demonstrated balanced performance across all metrics underscores its high potential as a report generation model that accurately conveys key content required in actual medical environments without distortion.

**Qualitative Results.** Fig. 3 presents a comparative example of automated report generation results based on chest CT images of a patient with suspected COVID-19 pneumonia. MedRegion-CT accurately identified bilateral GGO lesions and explicitly noted the absence of masses or nodules, thereby minimizing false-positive judgments. Clear performance differences among existing models were observed. M3D partially recognized the presence of diffuse GGO in bilateral lungs; however, it simultaneously exhibited errors of excessive localization to the lower lobes and inaccurate descriptions emphasizing the absence of nodules. MedBLIP and RadFM lacked specific descriptions of major lesions, omitting clear mention of GGO. In the case of CT2Rep, while it mentioned non-specific nodules, it failed to specify the key characteristic of ground-glass opacity and included unnecessary or false-positive findings such as emphysematous changes or linear atelectasis, which were inconsistent with the actual imaging findings. Based on comprehen-

sive analysis, our proposed model was evaluated to have enhanced clinical utility by most accurately reflecting clinically important information such as bilateral GGO and minimizing unnecessary lesion descriptions. This suggests that the proposed approach has the potential to generate consistent and reliable automated reports in cases of COVID-19 pneumonia.

### 4.3. Ablation Study

To evaluate the impact of individual components on the performance of our proposed model, we conducted ablation studies with various configurations. We experimented with four ablation variants: Ablation- $R^2$ +*Mask* (using  $R^2$  and masking mechanism), Ablation- $R^2$ +*Attr* (using  $R^2$  and attribute attention), Ablation- $R^2$  (using only the  $R^2$  component), and Ablation-*LITA* (using LITA method, uniformly sampling slices for slow tokens, instead of  $R^2$ ). The performance comparison between these variants and our complete model (Ours) is presented in Table 1 and Fig.3. As shown in Table 1, our complete model (Ours) consistently outperformed all ablation variants across various evaluation metrics. The complete model achieved the highest scores in BLEU-4 (0.290), ROUGE-L (0.375), CA (0.450), and GPT-4 score (48.837), demonstrating that optimal performance is achieved when all proposed components work synergistically. The Ablation-*LITA* demonstrated inferior performance compared to the Ablation- $R^2$  variant across LM-based evaluation metrics. These results provide evidence that  $R^2$  token pooling offers superior representational efficiency for volumetric feature extraction compared to uniform pooling strategies in the context of radiology report generation tasks. Ablation- $R^2$ +*Mask* showed performance similar to the complete model in BLEU-4 (0.280), but recorded slightly lower scores in CA (0.430) and GPT-4 score (44.457). This suggests that while the combination of  $R^2$  and masking mechanism contributes to structural accuracy, other components are also important for enhancing clinical accuracy. Interestingly, Ablation- $R^2$ +*Attr* showed a slightly higher value in BLEU-4 (0.293), but was lower than the complete model in CA (0.425) and GPT-4 score (47.319). This indicates that the combination of  $R^2$  and attribute attention may be advantageous for linguistic accuracy but does not fully guarantee clinical accuracy. Ablation- $R^2$  exhibited the lowest overall performance (BLEU-4: 0.261, METEOR: 0.481, ROUGE-L: 0.345, Green Score: 0.233, CA: 0.405, GPT-4 score: 43.014). This suggests that the  $R^2$  component alone has limitations in generating complex radiological reports without other complementary mechanisms. Fig.3 presents a qualitative comparison of reports generated for a COVID-19 pneumonia case, showing how each model configuration affects the clinical accuracy and comprehensiveness of the reports. Our complete model (Ours) accurately identi-

fied "diffuse ground-glass opacity densities" in "both lungs" and correctly interpreted it as "compatible with COVID-19 pneumonia." This aligns with the description in the ground truth report (GT) of "COVID-19 viral pneumonia" and "ground-glass opacities in both lungs." Similarly, Ablation- $R^2$ +*Mask* identified "diffuse ground-glass opacities" in "both lungs, especially the lower lobes," but did not mention an explicit association with COVID-19 pneumonia. Ablation- $R^2$ +*Attr* identified "diffuse ground-glass opacities" in "bilateral lower to mid lung zones" and interpreted this as "COVID-19 viral pneumonia," but unnecessarily recommended "clinical correlation and close follow-up.". The most notable difference was observed with Ablation- $R^2$ , which completely failed to identify ground-glass opacities and instead reported "normal aeration" and "no nodules or infiltrative lesions," presenting an interpretation entirely different from the actual findings. This severe performance degradation emphasizes that both *Attr* and *Mask* components are essential for accurately interpreting radiological findings.

## 5. Conclusion

In this work, we introduced **MedRegion-CT**, a region-focused MLLM framework for 3D chest CT report generation. By integrating  $R^2$  Token Pooling to balance global slice coverage with high-resolution local details, alongside a Mask-Driven Visual Extractor that handles pseudo-masks of major anatomical structures, our approach effectively captures both broad volumetric context and fine-grained regional information. Additionally, extracting Patient-Specific Attributes—such as organ volumes and lesion measurements—and converting them into textual prompts reduces ambiguity and improves clinical relevance. Experimental results on RadGenome-Chest CT demonstrate that MedRegion-CT outperforms baselines not only in linguistic fluency but also in diagnostic fidelity, underscoring the importance of region-centric cues for accurate and interpretable automated reporting. We anticipate future work can extend this structured, region-focused paradigm to other clinical imaging domains and more complex diagnostic scenarios, thereby further enhancing the reliability of AI-assisted medical reporting.

## References

- [1] Shah Hussain, Iqra Mubeen, Niamat Ullah, Syed Shahab Ud Din Shah, Bakhtawar Abduljalil Khan, Muhammad Zahoor, Riaz Ullah, Farhat Ali Khan, and Mujeeb A Sultan. Modern diagnostic imaging technique applications and risk factors in the medical field: a review. *BioMed research international*, 2022(1):5164970, 2022. 1
- [2] Stacy K Goergen, Felicity J Pool, Tari J Turner, Jane E Grimm, Mark N Appleyard, Carmel Crock, Michael C Fahy, Michael F Fay, Nicholas J Ferris, Susan M Liew, et al. Evidence-based guideline for the written radiology re-

- port: Methods, recommendations and implementation challenges. *Journal of medical imaging and radiation oncology*, 57(1):1–7, 2013. 1
- [3] Yann Erick Claessens, Marie-Pierre Debray, Florence Tubach, Anne Laure Brun, Blandine Rammaert, Pierre Hausfater, Jean-Marc Naccache, Patrick Ray, Christophe Choquet, Marie France Carette, Charles Mayaud, Catherine Leport, and Xavier Duval. Early chest computed tomography scan to assist diagnosis and guide treatment decision for suspected community-acquired pneumonia. *American journal of respiratory and critical care medicine*, 192 8:974–82, 2015. 1
- [4] Jean-Baptiste Alayrac, Jeff Donahue, Pauline Luc, Antoine Miech, Iain Barr, Yana Hasson, Karel Lenc, Arthur Mensch, Katherine Millican, Malcolm Reynolds, et al. Flamingo: a visual language model for few-shot learning. *Advances in neural information processing systems*, 35:23716–23736, 2022. 1
- [5] Junnan Li, Dongxu Li, Silvio Savarese, and Steven Hoi. Blip-2: Bootstrapping language-image pre-training with frozen image encoders and large language models. In *International conference on machine learning*, pages 19730–19742. PMLR, 2023.
- [6] Haotian Liu, Chunyuan Li, Qingyang Wu, and Yong Jae Lee. Visual instruction tuning. *Advances in neural information processing systems*, 36:34892–34916, 2023.
- [7] Zhiyu Wu, Xiaokang Chen, Zizheng Pan, Xingchao Liu, Wen Liu, Damai Dai, Huazuo Gao, Yiyang Ma, Chengyue Wu, Bingxuan Wang, et al. Deepseek-vl2: Mixture-of-experts vision-language models for advanced multimodal understanding. *arXiv preprint arXiv:2412.10302*, 2024.
- [8] Shuai Bai, Keqin Chen, Xuejing Liu, Jialin Wang, Wenbin Ge, Sibao Song, Kai Dang, Peng Wang, Shijie Wang, Jun Tang, et al. Qwen2. 5-vl technical report. *arXiv preprint arXiv:2502.13923*, 2025. 1
- [9] S. Kevin Zhou, Hayit Greenspan, Christos Davatzikos, James S. Duncan, Bram van Ginneken, Anant Madabhushi, Jerry L Prince, Daniel Rueckert, and Ronald M. Summers. A review of deep learning in medical imaging: Imaging traits, technology trends, case studies with progress highlights, and future promises. *Proceedings of the IEEE*, 109:820–838, 2020. 2
- [10] Martin J. Willeminck, Wojciech A Koszek, Cailin Hardell, Jie Wu, Dominik Fleischmann, Hugh Harvey, Les R. Folio, Ronald M. Summers, D. Rubin, and Matthew P. Lungren. Preparing medical imaging data for machine learning. *Radiology*, page 192224, 2020. 2
- [11] Ibrahim Ethem Hamamci, Sezgin Er, Furkan Almas, Ayse Gulnihan Simsek, Seval Nil Esirgun, Irem Dogan, Muhammed Furkan Dasdelen, Bastian Wittmann, Enis Simsar, Mehmet Simsar, et al. A foundation model utilizing chest ct volumes and radiology reports for supervised-level zero-shot detection of abnormalities. *CoRR*, 2024. 2
- [12] Xiaoman Zhang, Chaoyi Wu, Ziheng Zhao, Jiayu Lei, Ya Zhang, Yanfeng Wang, and Weidi Xie. Radgenome-chest ct: A grounded vision-language dataset for chest ct analysis. *arXiv preprint arXiv:2404.16754*, 2024. 2, 6
- [13] Chaoyi Wu, Xiaoman Zhang, Ya Zhang, Yanfeng Wang, and Weidi Xie. Towards generalist foundation model for radiology by leveraging web-scale 2d&3d medical data. *arXiv preprint arXiv:2308.02463*, 2023. 2, 3, 6
- [14] Qiuhui Chen and Yi Hong. Medblip: Bootstrapping language-image pre-training from 3d medical images and texts. In *Proceedings of the Asian Conference on Computer Vision*, pages 2404–2420, 2024. 3, 6, 2
- [15] Fan Bai, Yuxin Du, Tiejun Huang, Max Q-H Meng, and Bo Zhao. M3d: Advancing 3d medical image analysis with multi-modal large language models. *arXiv preprint arXiv:2404.00578*, 2024. 2, 3, 6
- [16] Ibrahim Ethem Hamamci, Sezgin Er, and Bjoern Menze. Ct2rep: Automated radiology report generation for 3d medical imaging. In *International Conference on Medical Image Computing and Computer-Assisted Intervention*, pages 476–486. Springer, 2024. 3, 6, 2
- [17] Ibrahim Ethem Hamamci, Sezgin Er, Furkan Almas, Ayse Gulnihan Simsek, Seval Nil Esirgun, Irem Dogan, Muhammed Furkan Dasdelen, Omer Faruk Durugol, Bastian Wittmann, Tamaz Amiranashvili, et al. Developing generalist foundation models from a multimodal dataset for 3d computed tomography. *arXiv preprint arXiv:2403.17834*, 2024. 2, 6
- [18] Sedigheh Eslami, Christoph Meinel, and Gerard De Melo. Pubmedclip: How much does clip benefit visual question answering in the medical domain? In *Findings of the Association for Computational Linguistics: EACL 2023*, pages 1181–1193, 2023. 2
- [19] Fernando Pérez-García, Harshita Sharma, Sam Bond-Taylor, Kenza Bouzid, Valentina Salvatelli, Maximilian Ilse, Shruthi Bannur, Daniel C Castro, Anton Schwaighofer, Matthew P Lungren, et al. Exploring scalable medical image encoders beyond text supervision. *Nature Machine Intelligence*, pages 1–12, 2025.
- [20] Xinrui Song, Xuanang Xu, and Pingkun Yan. General purpose image encoder dinov2 for medical image registration. *arXiv preprint arXiv:2402.15687*, 2024. 2
- [21] Liang Chen, Zekun Wang, Shuhuai Ren, Lei Li, Haozhe Zhao, Yunshui Li, Zefan Cai, Hongcheng Guo, Lei Zhang, Yizhe Xiong, et al. Next token prediction towards multimodal intelligence: A comprehensive survey. *arXiv preprint arXiv:2412.18619*, 2024. 2
- [22] Chunyuan Li, Cliff Wong, Sheng Zhang, Naoto Usuyama, Haotian Liu, Jianwei Yang, Tristan Naumann, Hoifung Poon, and Jianfeng Gao. Llava-med: Training a large language-and-vision assistant for biomedicine in one day. *Advances in Neural Information Processing Systems*, 36:28541–28564, 2023. 2
- [23] Omkar Thawkar, Abdelrahman Shaker, Sahal Shaji Mullappilly, Hisham Cholakkal, Rao Muhammad Anwer, Salman Khan, Jorma Laaksonen, and Fahad Shahbaz Khan. Xraygpt: Chest radiographs summarization using medical vision-language models. *arXiv preprint arXiv:2306.07971*, 2023.
- [24] Michael Moor, Qian Huang, Shirley Wu, Michihiro Yasunaga, Cyril Zalka, Yashodhara Dalmia, Eduardo Pontes Reis, Pranav Rajpurkar, and Jure Leskovec. Med-

- flamingo: a multimodal medical few-shot learner. *ArXiv*, abs/2307.15189, 2023.
- [25] Zhanyu Wang, Lingqiao Liu, Lei Wang, and Luping Zhou. R2gengpt: Radiology report generation with frozen llms. *Meta-Radiology*, 1(3):100033, 2023.
- [26] Kai Zhang, Jun Yu, Eashan Adhikarla, Rong Zhou, Zhiling Yan, Yixin Liu, Zhengliang Liu, Lifang He, Brian Davison, Xiang Li, et al. Biomedgpt: A unified and generalist biomedical generative pre-trained transformer for vision, language, and multimodal tasks. *arXiv e-prints*, pages arXiv–2305, 2023.
- [27] Zhihong Chen, Maya Varma, Jean-Benoit Delbrouck, Magdalini Paschali, Louis Blankemeier, Dave Van Veen, Jeya Maria Jose Valanarasu, Alaa Youssef, Joseph Paul Cohen, Eduardo Pontes Reis, et al. Chexagent: Towards a foundation model for chest x-ray interpretation. *arXiv preprint arXiv:2401.12208*, 2024.
- [28] Harshita Sharma, Valentina Salvatelli, Shaury Srivastav, Kenza Bouzid, Shruthi Bannur, Daniel C Castro, Maximilian Ilse, Sam Bond-Taylor, Mercy Prasanna Ranjit, Fabian Falck, et al. Maira-seg: Enhancing radiology report generation with segmentation-aware multimodal large language models. *arXiv preprint arXiv:2411.11362*, 2024. 3, 5
- [29] Tao Tu, Shekoofeh Azizi, Danny Driess, Mike Schaeckermann, Mohamed Amin, Pi-Chuan Chang, Andrew Carroll, Charles Lau, Ryutaro Tanno, Ira Ktena, et al. Towards generalist biomedical ai. *Nejm Ai*, 1(3):A10a2300138, 2024.
- [30] Yunfei Xie, Ce Zhou, Lang Gao, Juncheng Wu, Xianhang Li, Hong-Yu Zhou, Sheng Liu, Lei Xing, James Zou, Cihang Xie, et al. Medtrinity-25m: A large-scale multimodal dataset with multigranular annotations for medicine. *arXiv preprint arXiv:2408.02900*, 2024. 2
- [31] Jason J Lau, Soumya Gayen, Asma Ben Abacha, and Dina Demner-Fushman. A dataset of clinically generated visual questions and answers about radiology images. *Scientific data*, 5(1):1–10, 2018. 2
- [32] Alistair EW Johnson, Tom J Pollard, Seth J Berkowitz, Nathaniel R Greenbaum, Matthew P Lungren, Chih-ying Deng, Roger G Mark, and Steven Horng. Mimic-cxr, a de-identified publicly available database of chest radiographs with free-text reports. *Scientific data*, 6(1):317, 2019.
- [33] Xiaoman Zhang, Chaoyi Wu, Ziheng Zhao, Weixiong Lin, Ya Zhang, Yanfeng Wang, and Weidi Xie. Pmc-vqa: Visual instruction tuning for medical visual question answering. *arXiv preprint arXiv:2305.10415*, 2023. 2
- [34] Che Liu, Zhongwei Wan, Yuqi Wang, Hui Shen, Haozhe Wang, Kangyu Zheng, Mi Zhang, and Rossella Arcucci. Benchmarking and boosting radiology report generation for 3d high-resolution medical images. *arXiv preprint arXiv:2406.07146*, 2024. 3
- [35] Ibrahim Ethem Hamamci, Sezgin Er, Enis Simsar, Anjany Kumar Sekuboyina, Chinmay Prabhakar, Alperen Tezcan, Ayse Gulnihan Simsek, Sevval Nil Esirgun, Furkan Almas, Irem Dougan, Muhammed Furkan Dasdelen, Hadrien Reynaud, Sarthak Pati, Christian Bluethgen, Mehmet Kemal Ozdemir, and Bjoern H Menze. Generatect: Text-conditional generation of 3d chest ct volumes. In *European Conference on Computer Vision*, 2023. 3
- [36] Changsun Lee, Sangjoon Park, Cheong-II Shin, Woo Hee Choi, Hyun Jeong Park, Jeong Eun Lee, and Jong Chul Ye. Read like a radiologist: Efficient vision-language model for 3d medical imaging interpretation. *arXiv preprint arXiv:2412.13558*, 2024. 3
- [37] Yiming Shi, Xun Zhu, Ying Hu, Chenyi Guo, Miao Li, and Ji Wu. Med-2e3: A 2d-enhanced 3d medical multimodal large language model. *arXiv preprint arXiv:2411.12783*, 2024. 3
- [38] De-An Huang, Shijia Liao, Subhashree Radhakrishnan, Hongxu Yin, Pavlo Molchanov, Zhiding Yu, and Jan Kautz. Lita: Language instructed temporal-localization assistant. *ArXiv*, abs/2403.19046, 2024. 3, 5, 6
- [39] Mingze Xu, Mingfei Gao, Zhe Gan, Hong-You Chen, Zhengfeng Lai, Haiming Gang, Kai Kang, and Afshin Dehghan. Slowfast-llava: A strong training-free baseline for video large language models. *ArXiv*, abs/2407.15841, 2024.
- [40] Dabing Cheng, Haosen Zhan, Xingchen Zhao, Guisheng Liu, Zemin Li, Jinghui Xie, Zhao Song, Weiguo Feng, and Bingyue Peng. Text-to-edit: Controllable end-to-end video ad creation via multimodal llms. *ArXiv*, abs/2501.05884, 2025. 3
- [41] Christoph Feichtenhofer, Haoqi Fan, Jitendra Malik, and Kaiming He. Slowfast networks for video recognition. *2019 IEEE/CVF International Conference on Computer Vision (ICCV)*, pages 6201–6210, 2018. 3
- [42] Shilong Zhang, Pei Sun, Shoufa Chen, Min Xiao, Wenqi Shao, Wenwei Zhang, Kai Chen, and Ping Luo. Gpt4roi: Instruction tuning large language model on region-of-interest. *ArXiv*, abs/2307.03601, 2023. 3
- [43] Chuofan Ma, Yi Jiang, Jiannan Wu, Zehuan Yuan, and Xiaojuan Qi. Groma: Localized visual tokenization for grounding multimodal large language models. *ArXiv*, abs/2404.13013, 2024.
- [44] Qiushan Guo, Shalini De Mello, Hongxu Yin, Wonmin Byeon, Ka Chun Cheung, Yizhou Yu, Ping Luo, and Sifei Liu. Regiongpt: Towards region understanding vision language model. *2024 IEEE/CVF Conference on Computer Vision and Pattern Recognition (CVPR)*, pages 13796–13806, 2024. 3
- [45] Xiaoshuang Huang, Haifeng Huang, Lingdong Shen, Yehui Yang, Fangxin Shang, Junwei Liu, and Jia Liu. A refer-and-ground multimodal large language model for biomedicine. In *International Conference on Medical Image Computing and Computer-Assisted Intervention*, 2024. 3
- [46] Hong-Yu Zhou, Subathra Adithan, Julián Nicolás Acosta, Eric J. Topol, and Pranav Rajpurkar. A generalist learner for multifaceted medical image interpretation. *ArXiv*, abs/2405.07988, 2024.
- [47] Lehan Wang, Haonan Wang, Honglong Yang, Jiaji Mao, Zehong Yang, Jun Shen, and Xiaomeng Li. Interpretable bilingual multimodal large language model for diverse biomedical tasks. *ArXiv*, abs/2410.18387, 2024. 3
- [48] Shruthi Bannur, Kenza Bouzid, Daniel C. Castro, Anton Schwaighofer, Sam Bond-Taylor, Maximilian Ilse, Fernando P’erez-Garc’ia, Valentina Salvatelli, Harshita Sharma, Felix Meissen, Mercy Prasanna Ranjit, Shaury Srivastav, Julia

- Gong, Fabian Falck, Ozan Oktay, Anja Thieme, Matthew P. Lungren, Maria Teodora Wetscherek, Javier Alvarez-Valle, and Stephanie L. Hyland. Maira-2: Grounded radiology report generation. *ArXiv*, abs/2406.04449, 2024. 3
- [49] Tim Tanida, Philip Müller, Georgios Kaissis, and Daniel Rueckert. Interactive and explainable region-guided radiology report generation. *2023 IEEE/CVF Conference on Computer Vision and Pattern Recognition (CVPR)*, pages 7433–7442, 2023. 3
- [50] Lin Wang, Munan Ning, Donghuan Lu, Dong Wei, Yefeng Zheng, and Jie lian Chen. An inclusive task-aware framework for radiology report generation. In *International Conference on Medical Image Computing and Computer-Assisted Intervention*, 2022. 3
- [51] Yuqian Yuan, Wentong Li, Jian Liu, Dongqi Tang, Xinjie Luo, Chi Qin, Lei Zhang, and Jianke Zhu. Osprey: Pixel understanding with visual instruction tuning. *2024 IEEE/CVF Conference on Computer Vision and Pattern Recognition (CVPR)*, pages 28202–28211, 2023. 3, 5
- [52] Zhixuan Chen, Yequan Bie, Haibo Jin, and Hao Chen. Large language model with region-guided referring and grounding for ct report generation. *ArXiv*, abs/2411.15539, 2024. 3
- [53] Ziheng Zhao, Yao Zhang, Chaoyi Wu, Xiaoman Zhang, Ya Zhang, Yanfeng Wang, and Weidi Xie. One model to rule them all: Towards universal segmentation for medical images with text prompts. *ArXiv*, abs/2312.17183, 2023. 3, 6, 2
- [54] Pengfei Liu, Weizhe Yuan, Jinlan Fu, Zhengbao Jiang, Hiroaki Hayashi, and Graham Neubig. Pre-train, prompt, and predict: A systematic survey of prompting methods in natural language processing. *ACM Computing Surveys*, 55:1–35, 2021. 3
- [55] Yifan Li, Yifan Du, Kun Zhou, Jinpeng Wang, Wayne Xin Zhao, and Ji rong Wen. Evaluating object hallucination in large vision-language models. In *Conference on Empirical Methods in Natural Language Processing*, 2023. 3
- [56] Shengbang Tong, Zhuang Liu, Yuexiang Zhai, Yi Ma, Yann LeCun, and Saining Xie. Eyes wide shut? exploring the visual shortcomings of multimodal llms. *2024 IEEE/CVF Conference on Computer Vision and Pattern Recognition (CVPR)*, pages 9568–9578, 2024. 3
- [57] Ziyuan Qin, Huahui Yi, Qicheng Lao, and Kang Li. Medical image understanding with pretrained vision language models: A comprehensive study. *ArXiv*, abs/2209.15517, 2022. 4
- [58] Haibo Jin, Haoxuan Che, Yi-Mou Lin, and Haoxing Chen. Promptmrg: Diagnosis-driven prompts for medical report generation. *ArXiv*, abs/2308.12604, 2023. 4
- [59] Zhixuan Chen, Luyang Luo, Yequan Bie, and Hao Chen. Dia-llama: Towards large language model-driven ct report generation. *ArXiv*, abs/2403.16386, 2024. 4
- [60] Chun-Hsiao Yeh, Jiayun Wang, Andrew D. Graham, Andrea J. Liu, Bo Tan, Yubei Chen, Yi Ma, and Meng C. Lin. Insight: A multi-modal diagnostic pipeline using llms for ocular surface disease diagnosis. *ArXiv*, abs/2410.00292, 2024. 4, 5
- [61] Pedro R.A.S. Bassi, Mehmet Can Yavuz, Kang Wang, Xiaoxi Chen, Wenxuan Li, Sergio Decherchi, Andrea Cavalli, Yang Yang, Alan L. Yuille, and Zongwei Zhou. Radgpt: Constructing 3d image-text tumor datasets. *ArXiv*, abs/2501.04678, 2025. 4, 5
- [62] Peter Andrew Marcovici and George Albert Taylor. Journal club: Structured radiology reports are more complete and more effective than unstructured reports. *AJR. American journal of roentgenology*, 203 6:1265–71, 2014. 5
- [63] Lorenzo Cereser, Francesco Cortiula, C. Simiele, Valeria Peruzzi, Martina Bortolot, Annarita Tullio, Giuseppe Como, Chiara Zuiiani, and Rossano Girometti. Assessing the impact of structured reporting on learning how to report lung cancer staging ct: A triple cohort study on inexperienced readers. *European journal of radiology*, 171:111291, 2024. 5
- [64] Fernando P’erez-Garc’ia, Harshita Sharma, Sam Bond-Taylor, Kenza Bouzid, Valentina Salvatelli, Maximilian Ilse, Shruthi Bannur, Daniel C. Castro, Anton Schwaighofer, Matthew P. Lungren, Maria Teodora Wetscherek, Noel Codella, Stephanie L. Hyland, Javier Alvarez-Valle, and Ozan Oktay. Rad-dino: Exploring scalable medical image encoders beyond text supervision. *ArXiv*, abs/2401.10815, 2024. 5, 1
- [65] Salim Aymeric Si-Mohamed, Mouhamad Nasser, Marion Colevray, Olivier Nempont, Pierre Lartaud, Anna Sesilia Vlachomitrou, Thomas Broussaud, Kais Ahmad, Julie Traclet, Vincent Cottin, and Loic Boussel. Automatic quantitative computed tomography measurement of longitudinal lung volume loss in interstitial lung diseases. *European Radiology*, 32:4292–4303, 2022. 6
- [66] Shuai Ming, Wei Yang, Sijia Cui, Shuai Huang, and Xiangyang Gong. Consistency of radiologists in identifying pulmonary nodules based on low-dose computed tomography. *Journal of thoracic disease*, 11 7:2973–2980, 2019. 6
- [67] Hans Jonas Meyer, Alina Pfeil, Dominik Schramm, Andreas Gunter Bach, and Alexey Surov. Renal incidental findings on computed tomography. *Medicine*, 96, 2017. 6
- [68] Kishore Papineni, Salim Roukos, Todd Ward, and Wei-Jing Zhu. Bleu: a method for automatic evaluation of machine translation. In Pierre Isabelle, Eugene Charniak, and Dekang Lin, editors, *Proceedings of the 40th Annual Meeting of the Association for Computational Linguistics*, pages 311–318, Philadelphia, Pennsylvania, USA, July 2002. Association for Computational Linguistics. 6
- [69] Chin-Yew Lin. ROUGE: A package for automatic evaluation of summaries. In *Text Summarization Branches Out*, pages 74–81, Barcelona, Spain, July 2004. Association for Computational Linguistics. 6
- [70] Satanjeev Banerjee and Alon Lavie. Meteor: An automatic metric for mt evaluation with improved correlation with human judgments. In *IEEvaluation@ACL*, 2005. 6
- [71] An Yan, Julian McAuley, Xing Lu, Jiang Du, Eric Y. Chang, Amilcare Gentili, and Chun-Nan Hsu. Radbert: Adapting transformer-based language models to radiology. *Radiology. Artificial intelligence*, 4 4:e210258, 2022. 6
- [72] Sophie Ostmeier, Justin Xu, Zhihong Chen, Maya Varma, Louis Blankemeier, Christian Bluethgen, Arne Edward

Michalson, Michael E. Moseley, Curtis P. Langlotz, Akshay S. Chaudhari, and Jean-Benoit Delbrouck. Green: Generative radiology report evaluation and error notation. *ArXiv*, abs/2405.03595, 2024. [6](#)

- [73] Hugo Touvron, Thibaut Lavril, Gautier Izacard, Xavier Martinet, Marie-Anne Lachaux, Timothée Lacroix, Baptiste Rozière, Naman Goyal, Eric Hambro, Faisal Azhar, Aurélien Rodriguez, Armand Joulin, Edouard Grave, and Guillaume Lample. Llama: Open and efficient foundation language models. *ArXiv*, abs/2302.13971, 2023. [2](#)
- [74] J. Edward Hu, Yelong Shen, Phillip Wallis, Zeyuan Allen-Zhu, Yuanzhi Li, Shean Wang, and Weizhu Chen. Lora: Low-rank adaptation of large language models. *ArXiv*, abs/2106.09685, 2021. [2](#)
- [75] Ilya Loshchilov and Frank Hutter. Fixing weight decay regularization in adam. *ArXiv*, abs/1711.05101, 2017. [2](#)
- [76] Samyam Rajbhandari, Jeff Rasley, Olatunji Ruwase, and Yuxiong He. Zero: Memory optimizations toward training trillion parameter models. *SC20: International Conference for High Performance Computing, Networking, Storage and Analysis*, pages 1–16, 2019. [2](#)

# MedRegion-CT: Region-Focused Multimodal LLM for Comprehensive 3D CT Report Generation

## Supplementary Material

### 1. Patient Attribution Extractor

```
1: function GET_DIAMETER(mask)
2:   mask_array ←
3:     sitk.GetArrayFromImage(mask)
4:   labeled_mask ←
5:     skimimage.measure.label(mask_array)
6:   regions ←
7:     skimimage.measure.regionprops(labeled_mask)
8:   dmts ← ∅

9:   for rg in regions do
10:    mnz, mny, mnx, mxz, mxy, maxx ← rg.bbox
11:    dmts.append(
12:      max(maxx-mnx, mxy-mny, mxz-mnz)
13:    end for
14:   return dmts
15: end function

16: function COUNT_MASK(mask)
17:   mask_array ←
18:     sitk.GetArrayFromImage(mask)
19:   labeled_mask ←
20:     skimimage.measure.label(mask_array)
21:   num_objects ← max(labeled_mask)
22:   return num_objects
23: end function

24: for organ = [Lung, Heart, Liver, Kidney . . .] do
25:   volume ← sitk.GetArrayFromImage(organ).sum()
26: end for

27: for legion = [Nodule, Cyst, Effusion, . . .] do
28:   count ← COUNT_MASK(legion)
29:   diameter ← GET_DIAMETER(legion)
30:   location ← Filter by mask filename

31: end for
```

Figure 4. This code employs a deterministic algorithm to compute the volumes of multiple anatomical structures (e.g., lungs, liver, lesions) and to estimate the diameter of various pathological findings (e.g., nodules, cysts). The GET\_DIAMETER function determines the dimensional parameters of each lesion from the labeled masks.

### 2. Training and Implementation

**Training.** We preprocess the 3D CT images using consistent min-max normalization and resize the 3D images to

Input:

The global visual information is provided here: *<image>*.

The following regions of interest have been identified: lung*<region1>*,  
airway*<region2>*, ..., abdomen*<region6>*

Additional clinical attribute information is provided as follows:

Organ Volumes:

Lung:

- Right Upper Lobe: *{right\_upper\_lobe\_volume}* ml
- Right Middle Lobe: *{right\_middle\_lobe\_volume}* ml
- Right Lower Lobe: *{right\_lower\_lobe\_volume}* ml
- Left Upper Lobe: *{left\_upper\_lobe\_volume}* ml
- Left Lower Lobe: *{left\_lower\_lobe\_volume}* ml

Heart:

- Left Atrium: *{left\_atrium\_volume}* ml
- Right Atrium: *{right\_atrium\_volume}* ml
- Left Ventricle: *{left\_ventricle\_volume}* ml
- Right Ventricle: *{right\_ventricle\_volume}* ml

Liver: *{liver\_volume}* ml

Kidney:

- Left: *{left\_kidney\_volume}* ml
- Right: *{right\_kidney\_volume}* ml

Lesion Details:

Nodule:

- count: *{nodule\_count}*
- diameter (mm): *{nodule\_diameter}*
- location: *{nodule\_location}*

Cyst:

- count: *{cyst\_count}*
- diameter (mm): *{cyst\_diameter}*
- location: *{cyst\_location}*

Effusion:

- count: *{effusion\_count}*
- diameter (mm): *{effusion\_diameter}*
- location: *{effusion\_location}*

Describe this medical scan with findings.

Output:

```
[Lung]: {lung_findings}
[Airways]: {airways_findings}
[Mediastinum]: {mediastinum_findings}
[Heart]: {heart_findings}
[Osseous]: {osseous_findings}
[Abdomen]: {abdomen_findings}
```

Figure 5. The black text contains image information derived from CT slices, the blue text indicates region-specific segmentation tokens labeled as *<region i >*. The green text comprises attribute information extracted from (a), encompassing clinically relevant quantitative data. This text offers a structured presentation of volumes, counts, and locations of major organs and lesions identified in the medical scan. Based on these details, prompts can be provided for six distinct regions to generate corresponding clinical findings.

256 × 256 × 32 for input. We utilize RAD-DINO as our vision encoder and leverage its pre-trained image encoder checkpoint[64]. The vision encoder remains frozen during MLLM training. For the Multimodal Connector, we use a linear layer. For the generation of pseudo-masks, we used

the SAT [53] to extract major lesion and anatomical masks when unavailable. After  $R^2$  token pooling, the final 356 vision tokens are fed into the LLM. We utilize LLaMA3-8B [73] as our LLM base model and load its pre-trained parameters. The MLLM training consists of two steps. Initially, we froze the vision encoder and LLM while fine-tuning the Multimodal Connector with an image-report dataset, applying a batch size of  $4 \times 8$ , learning rate of  $10^{-4}$ , 3 epochs, with warmup and cosine decay. Subsequently, we fine-tune the Multimodal Connector, LLM, and segmentation module with structured report dataset, applying a batch size of  $1 \times 8$ , learning rate of  $2 \times 10^{-5}$ , 3 epochs, with warmup and cosine decay. For LLM fine-tuning, we consistently apply the parameter-efficient LoRA [74] method, with LoRA parameters set to  $r = 16$ ,  $\alpha = 32$ , and a dropout ratio of 0.1. The maximum sequence length for the LLM is set to 2,048. All models are trained using the AdamW [75] optimizer, and to optimize the training process, we leverage ZeRO [76] stage 2. The implementation is performed in PyTorch, and training is conducted in parallel on NVIDIA A100 GPUs with 80GB memory.

**Comparison.** For baseline comparisons, we compare three state-of-the-art open-source 3D methods capable of generating CT reports: RadFM [13], Med-BLIP [14], CT2Rep [16], and M3D [15]. To maintain consistency across methods, we used LLaMA3-8B [73] as the language decoder for all comparison methods. The input volumes are resized to  $256 \times 256 \times 32$ . Each compared model is either trained from scratch for models without pre-trained weights or initialized with pre-trained weights and further fine-tuned on the CT report generation dataset for models with pre-trained weights. Given resource limitations and to ensure a fair comparison, all experimental settings were controlled with a time constraint of 48 hours using two A100 GPUs for each experiment.